

Communication

High-Responsivity Planar Photodetector Based on Methylammonium Lead Bromide Perovskite Thin Film

Pavlo Mai, Julien Houel , Nathan Drevetton, Benoit Mahler  and Alban Gassenq *

Institut Lumière-Matière, CNRS UMR5306, Université Lyon 1, Université de Lyon, 69622 Villeurbanne, France

* Correspondence: alban.gassenq@univ-lyon1.fr

Abstract: We have fabricated planar interdigitated photodetectors exhibiting high responsivity. These detectors are based on thin layers of methylammonium lead bromide (MAPbBr₃) at 90 nm thickness. MAPbBr₃ thin films were first characterized on glass (borosilicate) substrates using absorption and photoluminescence measurements showing a high absorption edge at 521 nm and strong emission at 530 nm, as expected. MAPbBr₃ thin films were then deposited on top of interdigitated electrodes, hence producing planar photodetectors with responsivity up to 0.4 A/W. Such higher performances were attributed to the interdigitated design, low crack density (0.05 μm⁻²), and lower resistivity (20 MΩ.cm) compared to MAPbBr₃ single crystal. Therefore, this work highlights MAPbBr₃ thin films as very promising for photodetection applications.

Keywords: MAPbBr₃; photodetector; perovskite; responsivity

1. Introduction

Organic–inorganic hybrid perovskites (OIHPs) thin films based on methylammonium lead halide materials are widely studied for optoelectronics, including solar cells [1–3], light-emitting diodes [4], solar concentrators [5], scintillators [6], and photodetectors [7,8], since they present economical, fast, and easy fabrication processes as solutions [1,4,7,8]. For photodetectors, two designs are mainly studied: the vertical design [9–11] with an electric field (E-field) perpendicular to the layer and the horizontal design [12] with an E-field within the plane of the layer. For the horizontal configuration, the application of the E-field parallel to the substrate prevents short circuits that can potentially happen along the unavoidable thin-film cracks. Furthermore, it presents the advantage of simpler designs and processing by depositing the OIHP layers on top of patterned electrodes. For these reasons, many horizontal photodetectors have been studied for methylammonium lead iodide (MAPbI₃) [13,14], methylammonium lead chloride (MAPbCl₃) [15], or methylammonium lead bromide (MAPbBr₃) [16–23]. For MAPbBr₃, horizontal photodetectors have many advantages like room temperature crystallization and high stability and detection in the visible range [20–25]. They have been studied with transistor designs [22], micro-wires [26], single crystals [18,27], and thin films with face-to-face [20,28] or interdigitated electrodes [23]. In these cases, thin-layer MAPbBr₃ has very good properties for photodetection since they present perovskite structure with defects or doping, providing efficient carrier collection for photoconductive applications. For usual layers (without transistor designs [22]), responsivities are still limited to the maximal value of 55 mA/W [23] due to inhomogeneous layers [23] and the designs that do not use combs [20,28,29]. Such limitations can be attributed to the use of very small electrodes or non-homogeneous layers. Therefore, the development of high-quality MAPbBr₃ layers on top of larger electrodes such as the interdigitated comb design is highly needed to increase the responsivity of such promising detectors.

In this work, we report the fabrication of planar photodetectors based on 90 nm thick MAPbBr₃ layers. The layers were first characterized using absorption and photoluminescence measurements. Photodetectors based on interdigitated electrode combs were



Citation: Mai, P.; Houel, J.; Drevetton, N.; Mahler, B.; Gassenq, A. High-Responsivity Planar Photodetector Based on Methylammonium Lead Bromide Perovskite Thin Film. *Photonics* **2023**, *10*, 1043. <https://doi.org/10.3390/photonics10091043>

Received: 19 July 2023

Revised: 7 September 2023

Accepted: 12 September 2023

Published: 14 September 2023



Copyright: © 2023 by the authors. Licensee MDPI, Basel, Switzerland. This article is an open access article distributed under the terms and conditions of the Creative Commons Attribution (CC BY) license (<https://creativecommons.org/licenses/by/4.0/>).

then fabricated, with layers presenting low crack density. The spectral dependencies were measured for different wavelengths. Finally, in order to better understand the measured responsivity, electrical properties were investigated for different distances between the electrodes.

2. Materials and Methods

Figure 1a presents the process flow for the fabrication of planar photodetectors. Interdigitated combs [30] are first patterned using laser lithography (μ PG101, Heidelberg Instruments, Yokohama, Japan) with a GDS file on a BK7 substrate. A negative photoresist (AZ5214(En), MicroChemicals) was spin-coated at 3000 rpm and insolated at $50 \text{ mJ}/\text{cm}^2$ with 60 s development time. Cr/Au (10/300 nm) layers were then coated on top of the sample by sputtering deposition followed by lift-off processing using acetone. The period between the interdigitated electrodes is $8 \mu\text{m}$, and the distance is $4 \mu\text{m}$. Finally, the MAPbBr_3 thin film was deposited on top of the patterned substrate. MAPbBr_3 thin films were prepared following the anti-solvent method described in [31]. Briefly, 112 mg of methylammonium bromide (MABr, 99.8%, Sigma Aldrich, St. Louis, MO, USA) powder and 367 mg of lead bromide (99.999%, perovskite grade, Sigma Aldrich) were dissolved in 2 mL of anhydrous Dimethylformamide (DMF 98%, Sigma Aldrich), leading to a 0.5 M solution of MAPbBr_3 precursor. In total, 100 μL of that solution was drop-casted on a microscope coverslip (BK7) at 5000 rpm for 30 s. Five seconds after starting the spin coater, 500 μL of Chlorobenzene (99%, Sigma Aldrich) was injected to enforce the homogeneous crystallization of the MAPbBr_3 thin film. The result is a crystalline thin film with a thickness of 90 nm measured using atomic force microscopy (AFM).

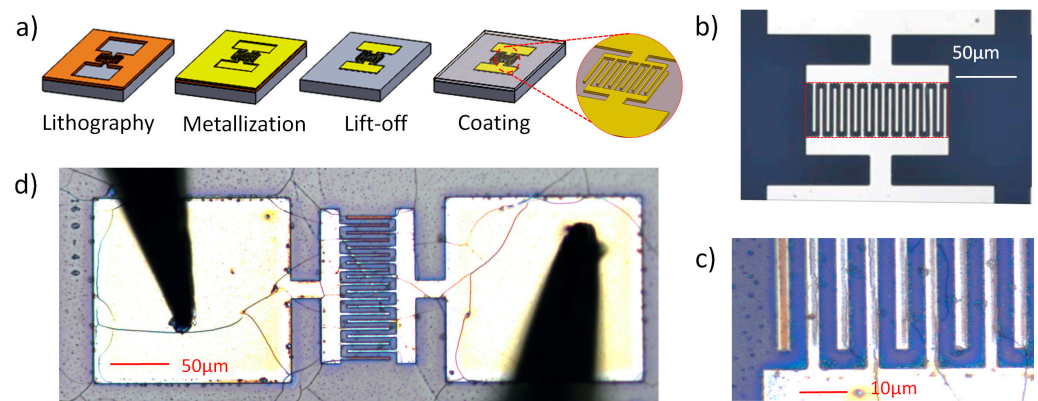


Figure 1. (a) Process flow for detector fabrication starting with lithography and metallization, followed by liftoff and film coating. Top image of fabricated photodetectors (b) after liftoff, (c) after the perovskite deposition, and (d) during the opto-electrical characterization.

Figure 1b–d present microscopic images of the fabricated photodetectors after the liftoff (Figure 1b), after coating (Figure 1c), and during electrical measurements (Figure 1d). As observed in Figure 1c,d, the layers are homogeneous since crack density has been typically evaluated at only 1 crack every $50 \mu\text{m}$ in the region of interest. Such linear crack density between the inter-digitated electrode gives a surface crack density of $0.05 \mu\text{m}^{-2}$. This value demonstrates good layer uniformity compared to other works [23].

3. Results

3.1. Perovskite Thin Layers

Figure 2 presents the optical properties of the studied layers deposited on the BK7 substrate without electrodes and measured using a spectrofluorometer (Edinburgh Instr., FS-5, Livingston, UK). Measurements were performed at room temperature. The photoluminescence measurement (Figure 2b) shows strong emission peaking at 530 nm with 20 nm full width half maximum. The shoulder peaks at around 550 nm can potentially

be attributed to active sub-bandgap defects, which are detected at wavelengths as long as 600 nm [32–34]. For the absorption spectrum (Figure 2a), the absorption exhibits an exciton peak at 521 nm, as expected from similar MAPbBr₃ thin films [35]. No significant signals were detected for longer wavelengths for both absorption and photoluminescence measurements.

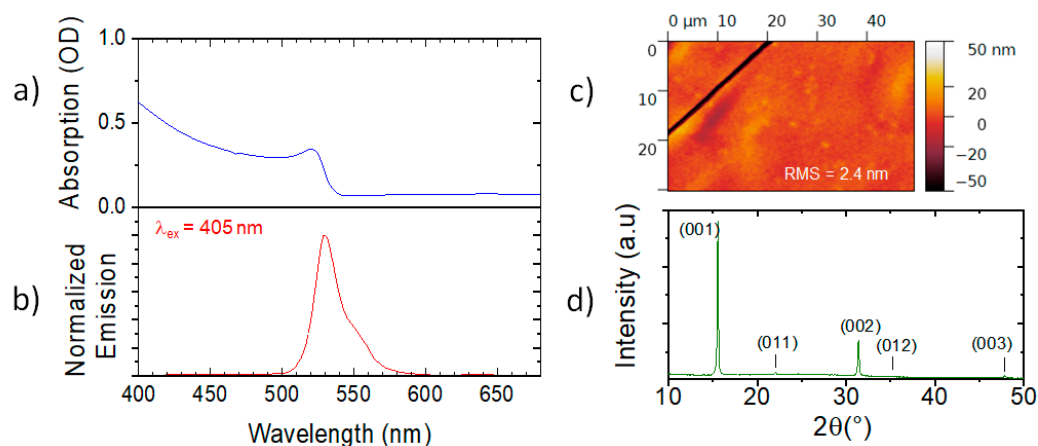


Figure 2. Optical properties of a MAPbBr₃ thin film on a BK7 substrate with its (a) absorption spectrum and (b) normalized photoluminescence excited at $\lambda_{exc} = 405$ nm. (c) AFM measurement for the MAPbBr₃ layer on SiO₂ showing low roughness relative to a detected crack and (d) XRD pattern of the film.

Figure 2c shows the topography of a film measured using Nanosurf Atomic Force Microscopy (AFM). AFM measurements were performed using Nanosurf-EasyScan2 equipment with a TAP190ALG-10 probe in tapping mode. A crack was observed on the left top corner, which enabled the determination of a film thickness of ~90 nm. The roughness value was measured relative to the cracks using Gwyddion software, giving a root mean square (RMS) value at 2.4 nm. Figure 2d presents the measured X-ray diffraction (XRD) of such films. A 2θ scan was performed using an AERIS PAN-analytic instrument from 5 to 45° and Cu-K α radiation at $\lambda = 15,406$ Å with a step size of 0.0109° and counting time of 40 s. XRD measurements confirm the fabrication of a monocrystalline film [36].

3.2. Photodetectors

Current versus voltage (I-V) curves were measured under illumination using a microscope (Eclipse LV100, Nikon), an electrical probe station, and a source/multimeter (2401, Keithley). In our study, $\times 10$ magnification and a 16 mm working distance were used to achieve enough distance between the objective and the contacted sample. Light power P was measured without the sample with a usual power meter. Figure 3a presents the I-V curves of the sample illuminated with the blue light spectrum presented in Figure 3b. The lamp spectra were measured using a fiber-coupled spectrometer (USB4000, Ocean optics), with the fiber replacing the microscope camera. The I-V curves under illumination were plotted with the colored full lines, and the I-V curve without light was plotted with black dashed lines. Firstly, we directly observe that almost no current is detected without light (~1 nA at 1 V), which confirms that the electrodes are not short-circuited. Under illumination, the current increases with light, and responsivity increases with voltage, as expected [16–18,20–23].

The responsivities R at 4 V and 0.125 W/cm^2 light excitation intensity have been extracted for three different wavelength ranges of excitations. The different spectra of the lamp used for this experiment are presented in Figure 3b–d with the corresponding responsivities. Responsivity R was calculated using the following formula:

$$R = \frac{I}{P \cdot S}, \tag{1}$$

where I is the detected photocurrent, S is the detector surface ($9720 \text{ }\mu\text{m}^2$ indicated by the red dashed line in Figure 1b), and P is the light power density (indicated in the inset of Figure 3a). The responsivities of 0.4, 0.05, and 0.03 A/W are measured for the spectra presented in Figure 3b–d, respectively. The influence of the excitation light was also investigated using long-pass filters placed in front of the detection path, with different cut-off wavelengths ranging from 400 to 700 nm. We present in Figure 3e the detected photocurrent as a function of the cut-off wavelength of the long-pass filters at 1 V using the lamp spectra presented in Figure 3c at 0.125 W/cm^2 light excitation intensity. The non-zero photocurrent detected for a cut-on wavelength at 600 nm is a signature of active sub-bandgap defects and intrinsic disorder in the Urbach tail of MAPbBr_3 , defects which are detected at wavelengths as long as 600 nm [31–34,37].

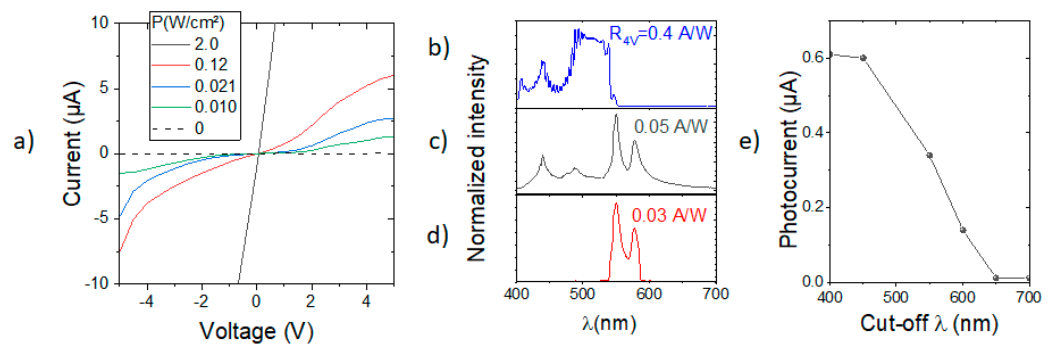


Figure 3. Opto-electrical characterization with the (a) I–V curve as a function of the light intensity for short wavelength light (blue light). Spectra and corresponding responsivities measured at 4 V for (b) short wavelength input light (blue light), (c) white light, and (d) long wavelength light (green light). (e) Wavelength dependence of the photocurrent as a function of the cut-on wavelength when a filter is placed on the beam path of the white lamp.

In order to better understand the responsivities measured in Figure 3, we have compared the photogenerated currents for different devices. The interdigitated combs with $4 \text{ }\mu\text{m}$ distance previously studied (Figure 4a) were compared to face-to-face electrode pads with a $200 \times 200 \text{ }\mu\text{m}^2$ surface and distances of $L = 45$ and $1260 \text{ }\mu\text{m}$ (Figure 4b). Figure 4c presents the averaged current (for a statistic over 10 measurements) as a function of the excitation light intensity for the three different designs, including interdigitate electrodes at 1 V polarization. Results are presented on a log scale to capture their full dynamics. Furthermore, layer resistivity ρ was also extracted from such data using the following equation:

$$\rho = \frac{D \cdot e}{L} \cdot r, \tag{2}$$

L is the distance between the electrodes, r is the measured resistance of the MAPbBr_3 thin film in between the electrodes, D is the effective width of the electrode (the values of D are indicated in Figure 4a,b, corresponding to the dashed red lines) and the thickness of the MAPbBr_3 thin film. We found a resistivity of $\rho = 25, 1,$ and $3 \text{ M}\Omega \cdot \text{cm}$ for $L = 4, 45,$ and $1260 \text{ }\mu\text{m}$, respectively.

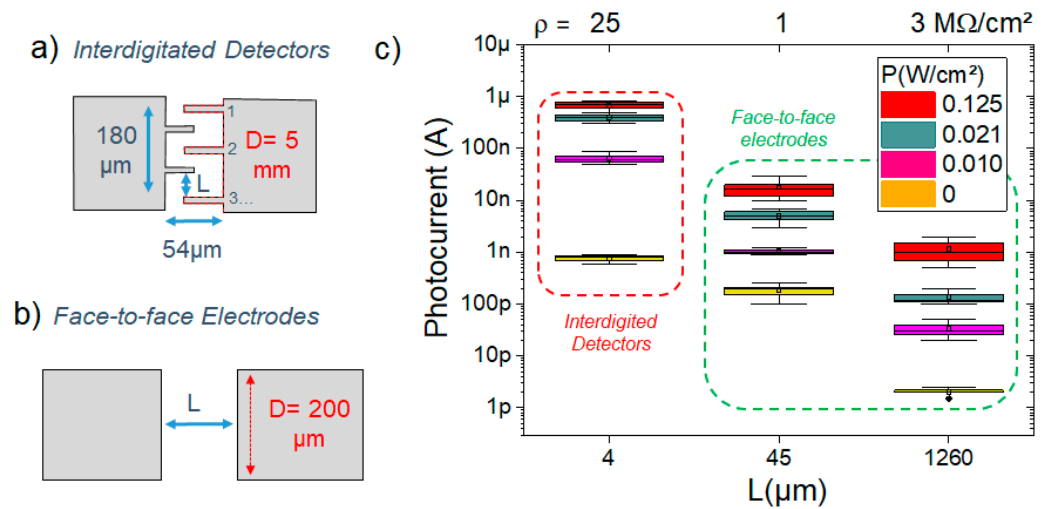


Figure 4. Schematic pictures for (a) the interdigitate and (b) face-to-face designs; (c) photocurrent as a function of the light intensity for both interdigitated and face-to-face designs at 1 V.

4. Discussion

As presented in Figure 3b, the highest responsivity is reported for blue light excitation since the absorption of the perovskite layer is high in this spectral region (Figure 1b). Furthermore, a higher photocurrent is also detected in Figure 3e for cut-on wavelengths below 500 nm (close to the MAPbBr₃ bandgap). The spectral behavior of the photoconductive devices is thus closely related to the layer’s properties, as expected. For suitable input light, a maximum responsivity of 0.4 A/W is demonstrated. Such a value is seven times higher than the highest values reported in the literature so far for similar devices due to our interdigitate design [20,21] and the better layer uniformity compared to [23].

To further understand such high responsivity, we can compare the different devices presented in Figure 4. We clearly see that the generated photocurrent is higher with the interdigitated electrodes ($L = 4 \mu\text{m}$ in Figure 4c) compared to the face-to-face electrodes ($L = 45$ and $1260 \mu\text{m}$ in Figure 4c) given the following responsivities: 0.1, 0.001, and 10^{-6} A/W for $L = 4, 45$ and $1260 \mu\text{m}$, respectively. Note that the interdigitated responsivity is lower than the one in Figure 3 because a voltage of only 1 V was used here, giving a minimum noise equivalent power of 10 nW. Therefore, the generated photocurrent appears to be highly related to the dark current. The charge collection is thus more efficient for the interdigitated electrodes compared to the face-to-face electrodes. Such tests confirm the interest in the interdigitate design. For resistivity (indicated at the top part of Figure 4c), comb resistivity ($L = 4 \mu\text{m}$) is higher compared to face-to-face designs with larger L distances, probably due to the Schottky barriers that have a higher influence on shorter distances [38]. Since no resistivity has been reported so far for MAPbBr₃ thin films in the literature, we can only compare these values with single-crystal MAPbBr₃ values. In this case, resistivity is lower than single crystals that are typically closer to $G\Omega\cdot\text{cm}$ [39]. This behavior could be attributed to the higher trap density acting as residual doping [9,40]. Therefore, this relatively larger dark current (usually associated with a limitation for photodiode detectors) coming from low resistivity is an advantage here for responsivity, especially for the interdigitated design. This work thus provides perspectives on intentional MAPbBr₃ doping [41,42] for detector applications.

5. Conclusions

As a conclusion, we have reported the fabrication of photodetectors based on interdigitated metallic combs with thin-film MAPbBr₃ of 90 nm thickness as active layers. With respect to the photodetector with comb designs, it exhibits high responsivity up to 0.4 A/W, which is seven times larger than similar devices from the state of the art in the literature, with a spectral dependence in good agreement with their optical properties. The highest

responsivity value was attributed to the comb design, low crack density ($0.05 \mu\text{m}^{-2}$), and relatively low resistivity ($25 \text{M}\Omega\cdot\text{cm}$) probably due to the high trap density, allowing good charge collection for photodetection. This work thus gives a better understanding of interdigitated devices with respect to MAPbBr_3 thin films used as active layers and highlights these thin layers as very promising candidates for the fast fabrication of economical devices for optoelectronic applications.

Author Contributions: Conceptualization, A.G. and J.H.; methodology, A.G., B.M. and P.M.; investigation, P.M. and N.D.; resources, B.M.; supervision A.G., B.M. and J.H.; writing—original draft preparation, A.G.; writing—review and editing, A.G. and J.H.; All authors have read and agreed to the published version of the manuscript.

Funding: This research has been funded by the Institute of Light Matter (UMR5306 CNRS UCBL).

Institutional Review Board Statement: Not applicable.

Informed Consent Statement: Not applicable.

Data Availability Statement: The data underlying the results presented in this paper are not publicly available at this time but may be obtained from the authors upon reasonable request.

Acknowledgments: The authors would like to thank the Nanolyon Platform for the clean room facilities. B.M. thanks the Université de Lyon PALSE program under the framework “Investissements d’avenir” (ANR-11-IDEX-0007).

Conflicts of Interest: The authors declare no conflict of interest.

References

1. Yang, W.S.; Park, B.W.; Jung, E.H.; Jeon, N.J.; Kim, Y.C.; Lee, D.U.; Seok, S.I. Iodide management in formamidinium-lead-halide-based perovskite layers for efficient solar cells. *Science* **2017**, *356*, 1376–1379. [[CrossRef](#)] [[PubMed](#)]
2. Mehdi, H.; Mhamdi, A.; Hannachi, R.; Bouazizi, A. MAPbBr_3 perovskite solar cells: Via a two-step deposition process. *RSC Adv.* **2019**, *9*, 12906–12912. [[CrossRef](#)]
3. Tang, M.C.; Dang, H.X.; Lee, S.; Barrit, D.; Munir, R.; Wang, K.; Li, R.; Smilgies, D.M.; De Wolf, S.; Kim, D.Y.; et al. Wide and Tunable Bandgap $\text{MAPbBr}_{3-x}\text{Cl}_x$ Hybrid Perovskites with Enhanced Phase Stability: In Situ Investigation and Photovoltaic Devices. *Sol. RRL* **2021**, *5*, 2000718. [[CrossRef](#)]
4. Ling, Y.; Yuan, Z.; Tian, Y.; Wang, X.; Wang, J.C.; Xin, Y.; Hanson, K.; Ma, B.; Gao, H. Bright Light-Emitting Diodes Based on Organometal Halide Perovskite Nanoplatelets. *Adv. Mater.* **2016**, *28*, 305–311. [[CrossRef](#)]
5. Zhou, Y.; Zhao, H.; Ma, D.; Rosei, F. Harnessing the properties of colloidal quantum dots in luminescent solar concentrators. *Chem. Soc. Rev.* **2018**, *47*, 5866–5890. [[CrossRef](#)] [[PubMed](#)]
6. Mykhaylyk, V.B.; Kraus, H.; Saliba, M. Bright and Fast Scintillation of Organolead Perovskite 479MAPbBr_3 at Low Temperatures. *Mater. Horiz.* **2019**, *6*, 1740–1747. [[CrossRef](#)]
7. Shrestha, S.; Fischer, R.; Matt, G.J.; Feldner, P.; Michel, T.; Osvet, A.; Levchuk, I.; Merle, B.; Golkar, S.; Chen, H.; et al. High-performance direct conversion X-ray detectors based on sintered hybrid lead triiodide perovskite wafers. *Nat. Photonics* **2017**, *11*, 436–440. [[CrossRef](#)]
8. Wu, X.; Zhou, B.; Zhou, J.; Chen, Y.; Chu, Y.; Huang, J. Distinguishable Detection of Ultraviolet, Visible, and Infrared Spectrum with High-Responsivity Perovskite-Based Flexible Photosensors. *Small* **2018**, *14*, 1800527. [[CrossRef](#)]
9. Yang, Z.; Deng, Y.; Zhang, X.; Wang, S.; Chen, H.; Yang, S.; Khurgin, J.; Fang, N.X.; Zhang, X.; Ma, R. High-performance single-crystalline perovskite thin-film photodetector. *Adv. Mater.* **2018**, *30*, 1704333. [[CrossRef](#)]
10. Chaudhary, J.; Choudhary, S.; Negi, C.M.S.; Gupta, S.K.; Verma, A.S. Surface morphological, optical and electrical characterization of methylammonium lead bromide perovskite ($\text{CH}_3\text{NH}_3\text{PbBr}_3$) thin film. *Phys. Scr.* **2019**, *94*, 105821. [[CrossRef](#)]
11. Xu, Z.; Zeng, Y.; Meng, F.; Gao, S.; Fan, S.; Liu, Y.; Zhang, Y.; Wageh, S.; Al-Ghamdi, A.A.; Xiao, J.; et al. A High-Performance Self-Powered Photodetector Based on MAPbBr_3 Single Crystal Thin Film/ MoS_2 Vertical Van Der Waals Heterostructure. *Adv. Mater. Interfaces* **2022**, *9*, 1–7. [[CrossRef](#)]
12. Wang, X.; Li, M.; Zhang, B.; Wang, H.; Zhao, Y.; Wang, B. Recent progress in organometal halide perovskite photodetectors. *Org. Electron.* **2018**, *52*, 172–183. [[CrossRef](#)]
13. Hu, W.; Cong, H.; Huang, W.; Huang, Y.; Chen, L.; Pan, A.; Xue, C. Germanium/perovskite heterostructure for high-performance and broadband photodetector from visible to infrared telecommunication band. *Light Sci. Appl.* **2019**, *8*, 106. [[CrossRef](#)]
14. Rong, S.S.; Faheem, M.B.; Li, Y.B. Perovskite single crystals: Synthesis, properties, and applications. *J. Electron. Sci. Technol.* **2021**, *19*, 1–18. [[CrossRef](#)]

15. Wang, W.; Xu, H.; Cai, J.; Zhu, J.; Ni, C.; Hong, F.; Fang, Z.; Xu, F.; Cui, S.; Xu, R.; et al. Visible blind ultraviolet photodetector based on $\text{CH}_3\text{NH}_3\text{PbCl}_3$ thin film. *Opt. Express* **2016**, *24*, 8411. [[CrossRef](#)] [[PubMed](#)]
16. Zhang, Z.; Chen, K.; Xia, W.; Zuo, Z. MAPbBr_3 single crystal based metal-semiconductor-metal photodetector enhanced by localized surface plasmon. *Mater. Res. Express* **2020**, *7*, 125902. [[CrossRef](#)]
17. Chen, L.C.; Lee, K.L.; Lee, K.Y.; Huang, Y.W.; Lin, R.M. Study of metal–semiconductor–metal $\text{CH}_3\text{NH}_3\text{PbBr}_3$ perovskite photodetectors prepared by inverse temperature crystallization method. *Sensors* **2020**, *20*, 297. [[CrossRef](#)]
18. Saidaminov, M.I.; Adinolfi, V.; Comin, R.; Abdelhady, A.L.; Peng, W.; Dursun, I.; Yuan, M.; Hoogland, S.; Sargent, E.H.; Bakr, O.M. Planar-integrated single-crystalline perovskite photodetectors. *Nat. Commun.* **2015**, *6*, 4–10. [[CrossRef](#)]
19. Gavranovic, S.; Pospisil, J.; Zmeskal, O.; Novak, V.; Vanysek, P.; Castkova, K.; Cihlar, J.; Weiter, M. Electrode Spacing as a Determinant of the Output Performance of Planar-Type Photodetectors Based on Methylammonium Lead Bromide Perovskite Single Crystals. *ACS Appl. Mater. Interfaces* **2022**, *14*, 20159–20167. [[CrossRef](#)]
20. Jang, D.M.; Park, K.; Kim, D.H.; Park, J.; Shojaei, F.; Kang, H.S.; Song, J.K. Reversible halide exchange reaction of organometal trihalide perovskite colloidal nanocrystals for full-range band gap tuning. *Nano Lett.* **2015**, *15*, 5191–5199. [[CrossRef](#)]
21. Choi, G.I.; Choi, H.W. A Study to Improve the Performance of Mixed Cation–Halide Perovskite-Based UVC Photodetectors. *Nanomaterials* **2022**, *12*, 1132. [[CrossRef](#)] [[PubMed](#)]
22. Yu, H.; Yan, L.; Qiu, R.; Xu, X.; Luo, W.; Zhou, H. Ambipolar solution-processed $\text{CH}_3\text{NH}_3\text{PbBr}_3$ perovskite phototransistors with ultra-thin Al_2O_3 protective layer. In Proceedings of the 2018 IEEE International Conference on Electron Devices and Solid State Circuits (EDSSC), Shenzhen, China, 6–8 June 2018; pp. 2–3.
23. Wang, F.; Mei, J.; Wang, Y.; Zhang, L.; Zhao, H.; Zhao, D. Fast photoconductive responses in organometal halide perovskite photodetectors. *ACS Appl. Mater. Interfaces* **2016**, *8*, 2840–2846. [[CrossRef](#)]
24. Zhou, S.; Wang, Q.; Xu, Z.; Xu, S.; Yang, P.; Deng, H.; Li, B.; Dong, Y.; Han, P.; Su, Y. Antisolvent solvothermal synthesis of MAPbBr_3 nanocrystals for efficient solar photodecomposition of methyl orange. *J. Colloid Interface Sci.* **2021**, *595*, 98–106. [[CrossRef](#)] [[PubMed](#)]
25. Zhu, Y.; Liu, Y.; Ai, Q.; Gao, G.; Yuan, L.; Fang, Q.; Lou, J. In situ synthesis of lead-free halide perovskite–COF nanocomposites as photocatalysts for photoinduced polymerization in both organic and aqueous phases. *ACS Mater. Lett.* **2022**, *4*, 464–471. [[CrossRef](#)]
26. Li, X.S.; Xu, Y.S.; Li, C.L.; Guo, Q.; Wang, G.; Xia, H.; Fang, H.H.; Shen, L.; Sun, H.B. Perovskite Single-Crystal Microwire-Array Photodetectors with Performance Stability beyond 1 Year. *Adv. Mater.* **2020**, *32*, 1–10. [[CrossRef](#)] [[PubMed](#)]
27. Zhang, Y.; Liu, Y.; Li, Y.; Yang, Z.; Liu, S. Perovskite $\text{CH}_3\text{NH}_3\text{Pb}(\text{Br}_x\text{I}_{1-x})_3$ single crystals with controlled composition for fine-tuned bandgap towards optimized optoelectronic applications. *J. Mater. Chem. C* **2016**, *4*, 9172–9178. [[CrossRef](#)]
28. Rahil, M.; Ansari, R.M.; Ahmad, S.; Islam, S.S. Nanostructured Ruddlesden–Popper-Layered Lead Bromide Perovskites with Stable and Selected Wavelength for Photodetection Applications. *ACS Appl. Nano Mater.* **2023**, *6*, 5187–5199. [[CrossRef](#)]
29. Shin, S.G.; Bark, C.W.; Choi, H.W. Study on performance improvements in perovskite-based ultraviolet sensors prepared using toluene antisolvent and $\text{CH}_3\text{NH}_3\text{Cl}$. *Nanomaterials* **2021**, *11*, 4. [[CrossRef](#)]
30. Gassenq, A.; Gencarelli, F.; Van Campenhout, J.; Shimura, Y.; Loo, R.; Narcy, G.; Roelkens, G. GeSn/Ge heterostructure short-wave infrared photodetectors on silicon. *Opt. Express* **2012**, *20*, 27297–27303. [[CrossRef](#)]
31. Baronnier, J.; Houel, J.; Dujardin, C.; Kulzer, F.; Mahler, B. Doping MAPbBr_3 hybrid perovskites with CdSe/CdZnS quantum dots: From emissive thin films to hybrid single-photon sources. *Nanoscale* **2022**, *14*, 5769–5781. [[CrossRef](#)]
32. Fu, J.; Jamaludin, N.F.; Wu, B.; Li, M.; Solanki, A.; Ng, Y.F.; Mhaisalkar, S.; Huan, C.H.A.; Sum, T.C. Localized Traps Limited Recombination in Lead Bromide Perovskites. *Adv. Energy Mater.* **2019**, *9*, 1803119. [[CrossRef](#)]
33. Baronnier, J.; Dujardin, C.; Mahler, B.; Houel, J. Low-Temperature Emission Dynamics of Methylammonium Lead Bromide Hybrid Perovskite Thin Films at the Sub-Micrometer Scale. *Nanomaterials* **2023**, *13*, 2376. [[CrossRef](#)] [[PubMed](#)]
34. Che, X.; Traore, B.; Katan, C.; Fang, H.H.; Loi, M.A.; Even, J.; Kepenekian, M. Charge Trap Formation and Passivation in Methylammonium Lead Tribromide. *J. Phys. Chem. C* **2019**, *123*, 13812–13817. [[CrossRef](#)]
35. Saidaminov, M.I.; Abdelhady, A.L.; Murali, B.; Alarousu, E.; Burlakov, V.M.; Peng, W.; Bakr, O.M. High-quality bulk hybrid perovskite single crystals within minutes by inverse temperature crystallization. *Nat. Commun.* **2015**, *6*, 7586. [[CrossRef](#)] [[PubMed](#)]
36. Wang, K.H.; Li, L.C.; Shellaiah, M.; Sun, K.W. Structural and Photophysical Properties of Methylammonium Lead Tribromide (MAPbBr_3) Single Crystals. *Sci. Rep.* **2017**, *7*, 13643. [[CrossRef](#)] [[PubMed](#)]
37. Droseros, N.; Tsokkou, D.; Banerji, N. Photophysics of Methylammonium Lead Tribromide Perovskite: Free Carriers, Excitons, and Sub-Bandgap States. *Adv. Energy Mater.* **2020**, *10*, 1903258. [[CrossRef](#)]
38. Hensch, H.K. Metal-semiconductor Schottky barrier junctions and their applications. *Proc. IEEE* **1986**, *74*, 894. [[CrossRef](#)]
39. Liu, X.; Fu, J.; Zhao, D.; Hao, Y.; Zhu, H.; Xu, M.; Xu, Y. $\text{MAPbBr}_{3-x}\text{I}_x$ Crystals Improved by Accurate Solution-Grown Procedure for Alpha Particle Detection. *Front. Phys.* **2020**, *7*, 1–6. [[CrossRef](#)]
40. Wenger, B.; Nayak, P.K.; Wen, X.; Kesava, S.V.; Noel, N.K.; Snaith, H.J. Consolidation of the optoelectronic properties of $\text{CH}_3\text{NH}_3\text{PbBr}_3$ perovskite single crystals. *Nat. Commun.* **2017**, *8*, 1. [[CrossRef](#)]

41. Ulatowski, A.M.; Wright, A.D.; Wenger, B.; Buizza, L.R.; Motti, S.G.; Eggimann, H.J.; Herz, L.M. Charge-Carrier Trapping Dynamics in Bismuth-Doped Thin Films of MAPbBr₃ Perovskite. *J. Phys. Chem. Lett.* **2020**, *11*, 3681–3688. [[CrossRef](#)]
42. Chatterjee, K.; Nayak, M.; Jahid Akhtar, A.; Saha, S.K. Sn doping enhanced current rectification in MAPbBr₃ nanocrystal-metal junction for photodetection. *Mater. Today Proc.* **2022**, *66*, 3205–3210. [[CrossRef](#)]

Disclaimer/Publisher's Note: The statements, opinions and data contained in all publications are solely those of the individual author(s) and contributor(s) and not of MDPI and/or the editor(s). MDPI and/or the editor(s) disclaim responsibility for any injury to people or property resulting from any ideas, methods, instructions or products referred to in the content.